RSC Advances

PAPER

View Article Online
View Journal | View Issue

Cite this: *RSC Adv.*, 2026, **16**, 14159

Robust and anti-swelling MXene composite hydrogel sensors for intelligent gait monitoring *via* a CNN-LSTM network

Qiujiang Wei,[a] Fuhuan Chu,[a] Chunyan Tian,[b] Hua Ke,[a] Xiya Wang,[a] Xiaomin Chen,[c] Linhui Qiang*[a] and Shiqi Xu *[a]

Received 16th December 2025
Accepted 5th March 2026

DOI: 10.1039/d5ra09713d

rsc.li/rsc-advances

Although flexible hydrogel sensors hold great promise in health monitoring, their reliability in long-term wearable scenarios is severely compromised by intrinsic hydrophilicity-induced uncontrollable swelling and signal drift. To address this critical bottleneck, we developed an MXene-poly(acrylic acid) (PAAc)-gelatin (MPG) composite hydrogel featuring superior anti-swelling properties. By incorporating Zr^{4+} coordination crosslinking, a robust "covalent-physical-coordination" triple network was constructed. This design not only endows the hydrogel with excellent mechanical toughness but also significantly restricts water uptake, achieving an ultralow 30-day cumulative swelling degree of 1.74%, thereby ensuring structural stability in humid environments. Based on this advanced material, a smart insole sensing system was fabricated. Benefiting from the high signal-to-noise-ratio and temporal stability of the MPG sensors, the proposed CNN-LSTM hybrid deep-learning model effectively extracts spatiotemporal features from complex gait signals. The system achieves a gait phase recognition accuracy of 88.0%, significantly outperforming conventional machine learning algorithms. This work demonstrates that the integration of high-performance anti-swelling materials with advanced deep learning algorithms represents an effective strategy for achieving next-generation precision wearable diagnostics.

Introduction

In recent years, flexible wearable sensors have attracted considerable attention owing to their broad potential in health monitoring, human–machine interaction, and rehabilitation engineering.[1–4] These devices enable real-time acquisition and intelligent analysis of diverse physiological signals, holding great promise for early disease diagnosis and motion performance evaluation. However, conventional sensors fabricated from metallic or silicon-based materials, although highly conductive, suffer from intrinsic brittleness and poor biocompatibility. Such deficiencies hinder their integration with soft tissues and restrict continuous operation under complex deformation environments.[5]

Hydrogels, characterized by their high water content and soft tissue-like modulus, have emerged as ideal candidates for next-generation flexible sensing matrices.[6–8] Nevertheless, traditional hydrogels typically rely on single physical or chemical cross-linking, resulting in loose polymer networks with poor mechanical strength.[9] Moreover, their high water content often induces undesirable swelling and deswelling behaviors, which disrupt conductive pathways and lead to signal drift over time.[10] Although strategies such as introducing secondary cross-linkers have been explored, achieving a simultaneous optimization of mechanical robustness, sensitivity, and long-term durability remains a significant challenge.[11–13]

Among various polymer matrices, poly(acrylic acid) (PAAc) has shown excellent potential due to its abundant carboxyl groups, which facilitate dynamic cross-linking *via* hydrogen bonding and ionic coordination.[14] Recent studies have demonstrated that PAAc-based hydrogels, when reinforced with nanocomponents[15] or metal ion coordination (*e.g.*, Zr^{4+}),[16] can achieve remarkable mechanical integrity and self-healing capabilities. However, utilizing PAAc alone often falls short in meeting the stringent requirements for anti-swelling performance and biocompatibility required for long-term skin-contact applications.

To address this, bio-based polymers like gelatin have gained traction.[17–19] Gelatin can form reversible hydrogen-bonded networks and, notably, coordinate with metal ions to significantly enhance stiffness and thermostability.[20,21] This coordination-driven reinforcement is crucial for imparting anti-swelling capabilities. In parallel, two-dimensional MXene ($Ti_3C_2T_x$) nanosheets have emerged as ideal conductive fillers owing to their excellent electrical conductivity and hydrophilicity.[22–24] Previous works have indicated that

[a]*Hebei International Research Center for Medical-Engineering, Chengde Medical University, Chengde 067000, China. E-mail: qianglinhui@163.com; xushiqi@cdmc.edu.cn*

[b]*Chongqing Health Vocational College, Chongqing 402260, China*

[c]*School of Artificial Intelligence, Shandong Xiandai University, Jinan 250000, China*

integrating PAAc, gelatin, and MXene provides a rational pathway to construct hydrogels combining toughness, swelling resistance, and conductivity.[25]

Despite these material-level advancements, signal interpretation remains a bottleneck. The signals collected from flexible sensors are multidimensional, nonlinear, and subject-dependent.[26–28] With the advent of artificial intelligence, deep learning has emerged as a transformative tool for extracting features from biosensor data.[29] While studies have successfully employed Convolutional Neural Networks (CNNs)[30] or Long Short-Term Memory (LSTM) networks[31] for gesture recognition, hybrid neural architectures that jointly capture local spatial features and global temporal dependencies in gait analysis remain underexplored.

In this context, the present work reports an anti-swelling MXene-poly(acrylic acid) (PAAc)-gelatin (MPG) composite hydrogel sensor. Designed *via* a synergistic covalent-physical-coordination cross-linking strategy, the hydrogel simultaneously exhibits enhanced mechanical flexibility, electrical stability, and volumetric integrity. The sensor was integrated into a smart insole system for real-time plantar pressure monitoring. Furthermore, a CNN-LSTM hybrid deep learning model was developed to effectively extract spatiotemporal features from the sensor output, achieving an average classification accuracy of 88.0%. This study establishes a comprehensive framework coupling anti-swelling hydrogels with deep learning interpretation, providing a new paradigm for intelligent wearable diagnostics.

Results and discussion

Synthesis and formation mechanism of MXene-PAAc-gelatin hydrogel

The synthesis route of MXene nanosheets is illustrated in Fig. 1a. High-quality $Ti_3C_2T_x$ MXene was prepared by selectively etching the Al atomic layers from the Ti_3AlC_2 MAX phase in an HCl-LiF mixed solution. As evidenced by scanning electron microscopy (SEM), the etched MXene exhibited a characteristic loose accordion-like morphology (Fig. 1c). The enlarged interlayer spacing, resulting from Li^+ intercalation and Al removal, provided favorable conditions for subsequent ultrasonic exfoliation, yielding few-layer or single-layer MXene nanosheets with high aspect ratios (Fig. 1d). The structural evolution was further elucidated by X-ray diffraction (XRD) patterns (Fig. 1f). Compared with the pristine Ti_3AlC_2 phase, the complete disappearance of the (104) diffraction peak at 39° confirmed the effective removal of Al layers. Concurrently, the (002) peak shifted significantly from 9.52° to 6.66°, indicating a pronounced expansion of the interlayer distance (*d*-spacing), which is consistent with the successful transformation into two-dimensional $Ti_3C_2T_x$ lamellae.[32] Furthermore, X-ray photoelectron spectroscopy (XPS) survey analysis (Fig. 1g) verified the surface elemental composition. The characteristic peaks of Ti, C, O, and F were clearly observed. Specifically, the distinct signals for O 1s and F 1s confirmed the successful introduction of abundant hydrophilic surface terminations (=O, –OH, and –F) on the $Ti_3C_2T_x$ nanosheets.[33] These surface functional groups are critical, as they provide active sites for forming strong interfacial coordination with the polymer matrix in the subsequent hydrogel synthesis.

Building upon the exfoliated MXene, the high-performance MPG composite hydrogel was synthesized through a facile one-pot radical polymerization strategy, as illustrated in Fig. 2. During this process, acrylic acid (AAc) monomers underwent *in situ* free-radical polymerization to form long poly(acrylic acid) (PAAc) chains, which served as the primary covalent backbone of the hydrogel network.[34] Simultaneously, the introduced gelatin chains interpenetrated the PAAc matrix, establishing a reversible physical network *via* extensive hydrogen bonding and electrostatic interactions. These physical entanglements not only enhanced the mechanical toughness and energy dissipation of the hydrogel but also restricted the movement of polymer chains.[35] More importantly, Zr^{4+} ions acted as powerful coordination centers, cross-linking with the carboxyl groups (–COOH) of PAAc and the oxygen-containing groups on the MXene surface. This high-density coordination, combined with

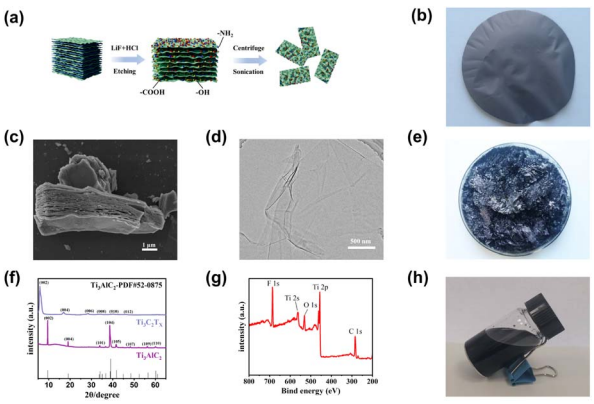

Fig. 1 (a) Preparation flowchart of MXene, (b) self-supporting MXene film, (c) SEM image of MXene nanosheets exhibiting a typical accordion-like layered structure, (d) TEM image of a delaminated single-layer MXene nanosheet, confirming the successful exfoliation into monolayer flakes, (e) photograph of freeze-dried flocculent MXene, (f) XRD patterns of the MAX precursor and the obtained MXene, (g) XPS survey spectrum of MXene showing the elemental composition, (h) photograph of the MXene dispersion.

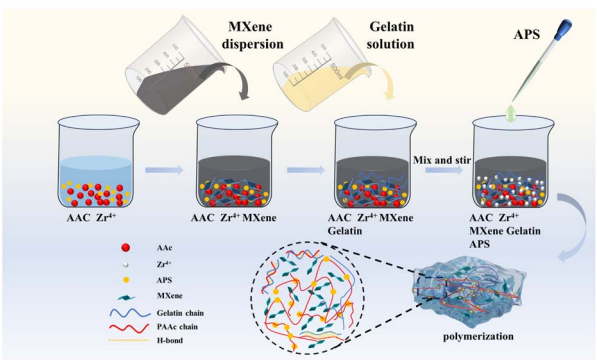

Fig. 2 Schematic of the preparation process of MPG hydrogels as well as the polymerization mechanism diagram.

the rigid support of MXene nanosheets, created a robust "dual-locking" effect that effectively densified the network structure. Consequently, a hierarchical "covalent–physical–coordination" interpenetrating network was successfully constructed. This synergistic architecture endowed the MPG hydrogel with an exceptional combination of mechanical robustness, stable electrical conductivity, and, crucially, superior anti-swelling capability by suppressing the osmotic pressure-driven expansion of polymer chains.[36]

Fundamental properties of MXene-PAAc-gelatin hydrogels

The fundamental properties of the MPG composite hydrogel play a pivotal role in determining its practical performance as a flexible wearable pressure sensor. The mechanical behavior governs the structural integrity of the device under tensile or compressive deformation, serving as a prerequisite for stable signal output. The electrical characteristics directly affect the sensor's sensitivity and signal transmission efficiency, while the swelling behavior reflects the long-term environmental stability of the hydrogel, particularly under humid or physiological conditions. Excessive water absorption can lead to network relaxation, degradation of mechanical strength, and disruption of conductive pathways.[37]

To systematically evaluate the influence of MXene content on the integrated performance of the composite system, a series of hydrogels containing different MXene concentrations (0, 2, 4, 6, 8, and 10 mg mL^{-1}) were synthesized. Their chemical composition, micromorphology, mechanical properties, electrical conductivity, and swelling resistance were comprehensively characterized and compared (Fig. 3 and 4).

Morphological and chemical characterization. To verify the formation of the proposed "covalent–physical–coordination" triple network, X-ray photoelectron spectroscopy (XPS) was employed to analyze the chemical states of the optimized MPG hydrogel (6 mg mL^{-1}). As presented in Fig. 3g, the high-resolution C 1s spectrum is deconvoluted into three distinct peaks at 284.8 eV (C–C), 286.35 eV (C–O–C), and 288.45 eV (O–C=O), corresponding to the carbon backbone of PAAc and gelatin.

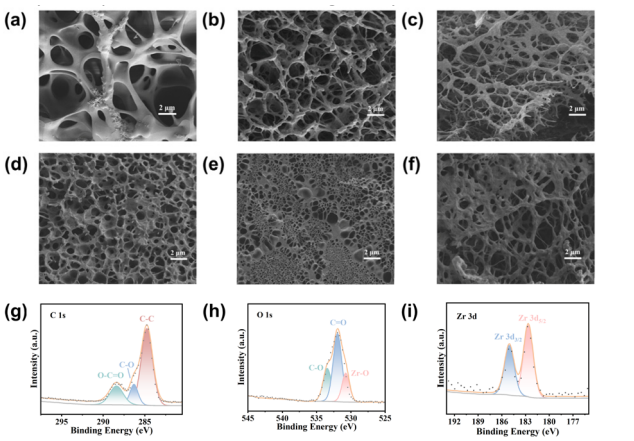

Fig. 3 SEM images of freeze-dried hydrogels with different MXene contents: (a) 0 mg mL^{-1}, (b) 2 mg mL^{-1}, (c) 4 mg mL^{-1}, (d) 6 mg mL^{-1}, (e) 8 mg mL^{-1}, and (f) 10 mg mL^{-1}. High-resolution XPS spectra of the optimized hydrogel: (g) C 1s, (h) O 1s, and (i) Zr 3d.

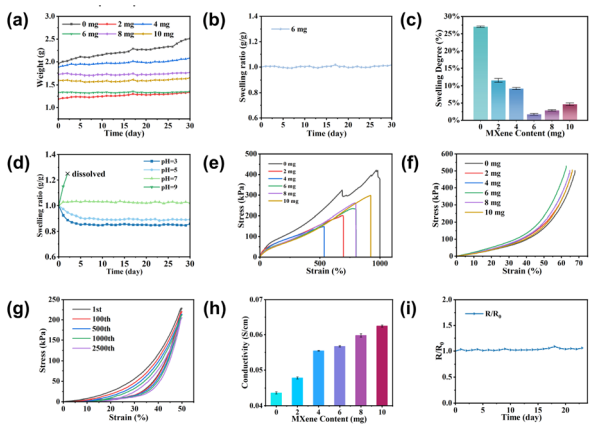

Fig. 4 (a) Weight variation of hydrogels with different MXene contents over 30 days, (b) swelling ratio of the optimized hydrogel (6 mg mL^{-1}) over 30 days, (c) swelling degrees of hydrogels with various MXene concentrations, (d) swelling behavior in different pH solutions, (e) tensile stress–strain curves, (f) compressive stress–strain curves, (g) cyclic compressive stress–strain curves for 2500 cycles, (h) electrical conductivity *versus* MXene content, (i) resistance stability of the hydrogel sensor under high temperature and high humidity conditions for 24 h.

Crucially, the O 1s spectrum (Fig. 3h) provides direct evidence of the metal-polymer coordination. Unlike pure organic hydrogels which typically exhibit only organic oxygen signals, the O 1s spectrum of the MPG hydrogel reveals a distinct component at a lower binding energy. The peak located at 530.75 eV is characteristic of the Zr–O bond formed through coordination, which is distinct from the C=O (531.95 eV) and C–O (533.45 eV) species.[38] The emergence of this specific peak confirms that the Zr^{4+} ions have successfully coordinated with the carboxyl groups of PAAc and surface groups of MXene, as the lattice oxygen in zirconium-based clusters typically appears in this region. Furthermore, the Zr 3d spectrum (Fig. 3i) displays a standard doublet at 182.65 eV ($Zr\ 3d_{5/2}$) and 185.05 eV ($Zr\ 3d_{3/2}$). The binding energy values and the spin–orbit splitting of 2.4 eV are consistent with the standard values for Zr(IV) reported in the XPS handbook,[39] corroborating the formation of stable coordination crosslinks within the hydrogel network.

The influence of this chemical architecture on the micromorphology is visualized in Fig. 3a–f. The pristine PAAc hydrogel (Fig. 3a) exhibits a honeycomb-like structure with smooth but relatively thin pore walls, indicating a loose network. Upon incorporating MXene (Fig. 3b–d), the pore walls become progressively thicker and more rugged, suggesting that the nanosheets are uniformly embedded within the matrix and act as physical crosslinkers to densify the framework. Specifically, at the optimal concentration of 6 mg mL^{-1} (Fig. 3d), the hydrogel displays a highly interconnected and robust porous structure, which facilitates efficient stress transfer and electron transport. However, when the MXene content exceeds

8 mg mL^{-1} (Fig. 3e–f), localized aggregation of nanosheets is observed, which partially blocks the pores and may disrupt the structural homogeneity.[40]

Integration of environmental stability and mechanical robustness. The practical application of wearable sensors necessitates a rigorous material screening process to balance environmental stability, mechanical compliance, and electrical conductivity. Gravimetric stability in aqueous environments served as the primary screening criterion. As shown in Fig. 4c, the introduction of MXene significantly suppressed the water uptake capacity.

To further verify long-term reliability, the mass variation of the hydrogels in deionized water (25 °C) was monitored over a period of 30 days (Fig. 4a). The results reveal a distinct divergence: while the pristine hydrogel and low-loading samples (0–2 mg mL^{-1}) underwent continuous volume expansion with no sign of thermodynamic equilibrium, the optimized 6 mg mL^{-1} sample rapidly reached a stable plateau. As shown in Fig. 4b, the normalized swelling ratio (W_t/W_0) of the 6 mg mL^{-1} hydrogel remained highly stable, fluctuating negligibly around 1.0 throughout the 30-day immersion. Ultimately, the cumulative swelling degree after 30 days was merely 1.74% (Fig. 4c), confirming exceptional resistance to hydrolytic swelling.

This improvement is attributed to a "Dual-Locking" mechanism induced by the MXene network.[25,36,41] Specifically, the rigid 2D MXene nanosheets function as physical crosslinkers that effectively densify the triple network, thereby restricting the relaxation and mobility of polymer chains.[25,41] Simultaneously, the abundant surface functional groups (–OH, –F) on MXene facilitate the formation of strong hydrogen bonds and coordination complexes with Zr^{4+}.[36] This chemically anchored high-density network significantly increases the elastic retraction force, which effectively counteracts the osmotic pressure driving water absorption and ensures superior dimensional stability.

Furthermore, this stability was validated across a physiological pH range (Fig. 4d). The hydrogel exhibited excellent structural integrity in acidic (pH 3) and neutral (pH 5, 7) environments. This stability stems from the pH-responsive nature of PAAc chains. In acidic and near-neutral environments, carboxyl groups ($–COO^-$) are protonated (–COOH), promoting hydrogen bonding and chain aggregation, thereby "locking" the network structure. However, under alkaline conditions (pH 9), the hydrogel exhibited significant swelling and partial degradation. This is attributed to the deprotonation of carboxyl groups, which induces strong electrostatic repulsion between intra- and inter-molecular chains (polyelectrolyte effect), leading to network expansion and dissociation.[42] Nevertheless, the exceptional gravimetric stability within the pH 3–7 range confirms the sensor's suitability for wearable applications involving contact with human sweat (typically pH 4–7).

In terms of mechanical properties, the –OH and –F functional groups on the MXene surface interact with the carboxyl groups of PAAc and Zr^{4+} ions through hydrogen bonding and coordination, thereby constructing a robust multi-level "covalent–physical–coordination" crosslinking network. Based on this architecture, the hydrogel exhibited superior mechanical performance.[43] Tensile tests (Fig. 4e) showed that the 6 mg mL^{-1} hydrogel achieved an ideal balance—maintaining high elongation ($\approx$800%) and adequate tensile strength (0.235 MPa) while avoiding the brittleness observed at high loadings. For plantar pressure applications, compressive resilience is critical. As shown in Fig. 4f, under 0.5 MPa pressure, the 6 mg mL^{-1} sample exhibited the highest compressive modulus, indicating superior compressive stiffness without structural collapse. Its structural durability was further verified by cyclic fatigue tests (Fig. 4g): over 2500 loading–unloading cycles, the stress–strain hysteresis loops remained highly overlapped, indicating negligible plastic deformation and excellent elasticity.

Electrical conductivity is another critical parameter. As shown in Fig. 4h, the conductivity exhibits a linear increase with rising MXene content, attributed to the formation of effective electron transport channels by the uniformly dispersed nanosheets. However, in flexible sensing applications, higher conductivity does not strictly equate to better overall performance. Excessive filler loading often compromises mechanical homogeneity. Simultaneously, excessively high conductivity can diminish the dynamic resolution of the sensing signal, as minor resistance variations become indistinguishable under near-saturated conductive states.[44] Consequently, the 6 mg mL^{-1} formulation was identified as the ideal candidate, offering moderate conductivity (0.056 S cm^{-1}) balanced with superior mechanical uniformity. Finally, the baseline resistance stability was evaluated (Fig. 4i). Under high temperature and high humidity conditions (37 °C, 90% RH), the initial resistance (R_0) remained stable with no significant drift. This confirms the hydrogel's exceptional environmental adaptability, derived from its intrinsic anti-swelling capability. The above results indicate that the 6 mg mL^{-1} composition achieves the optimal balance among stability, mechanical performance, and electrical properties.

Sensing performance of MXene-PAAc hydrogel-based sensor

The sensing performance serves as a critical determinant for the high-sensitivity detection capability of flexible wearable pressure sensors. In particular, sensitivity (S) quantifies the device's responsiveness to external pressure variations, while response and recovery times reflect its dynamic sensing behavior and temporal resolution.[45] To systematically evaluate the influence of MXene concentration on the overall sensing characteristics, a series of hydrogel-based sensors incorporating varying MXene contents (0, 2, 4, 6, 8, and 10 mg mL^{-1}) were fabricated and comparatively analyzed.

As summarized in Fig. 5a, the response and recovery speeds improved significantly with the incorporation of MXene. The pristine PAAc hydrogel exhibited prolonged response and recovery times of 555 ms and 580 ms, respectively, attributed to the inherent viscoelastic retardation of the pure polymer network. In contrast, the introduction of MXene constructed efficient electron transport pathways, enabling rapid signal transduction. Notably, the 6 mg mL^{-1} sample (Fig. 5b) achieved the fastest dynamic response (92/129 ms), facilitating real-time capture of transient mechanical signals. However, further

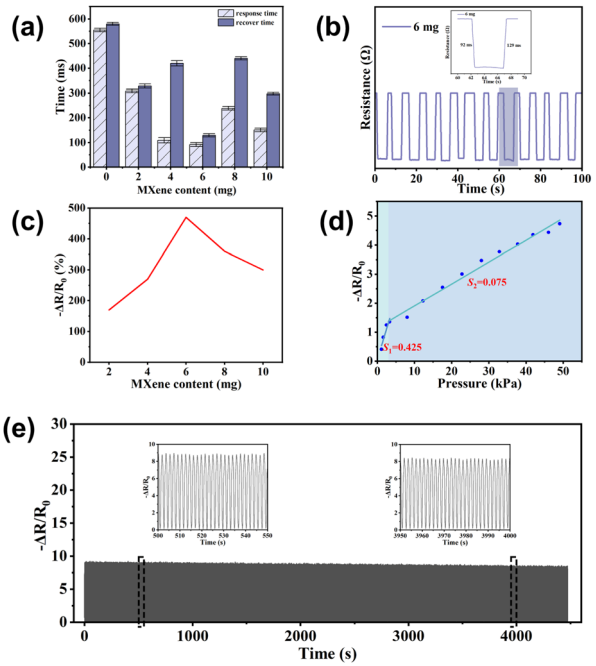

Fig. 5 (a) Response and recovery times of hydrogels with different MXene contents, (b) dynamic resistance response of the hydrogel sensor containing 6 mg of MXene, showing a response time of 92 ms and a recovery time of 129 ms, (c) relative resistance change ($-\Delta R/R_0$) of hydrogels with varying MXene contents, (d) fitted segmented sensitivity curves (S) derived from the $-\Delta R/R_0$ *versus* pressure relationship, (e) long-term cyclic stability test under repeated loading and unloading cycles.

increasing the loading to 8–10 mg mL^{-1} resulted in a slight sluggishness. This reversal is likely due to the agglomeration of excess nanosheets, which disrupts the continuity of the conductive network and introduces steric hindrance to ion migration.[46]

The relative resistance change under a fixed pressure of 50 kPa (Fig. 5c) further elucidates the composition-performance relationship. The sensor response exhibits a volcano-shaped trend, peaking at the 6 mg mL^{-1} concentration with a maximum response of 470%—more than double that of the pristine sample 170%). This enhancement confirms that 6 mg mL^{-1} represents the optimal percolation threshold, where a homogeneous and robust conductive network is established within the PAAc matrix. This architecture allows minute structural deformations to be efficiently amplified into detectable resistance variations. Conversely, excessive loading leads to filler aggregation, which compromises the effective stress transfer and reduces the signal-to-noise ratio.[47]

Based on the optimized response speed and signal amplitude, the 6 mg mL^{-1} hydrogel was selected for detailed sensitivity analysis. As shown in Fig. 5d, the sensor displays a characteristic dual-linear regime: a high sensitivity of $S_1 = 0.425$ kPa^{-1} in the low-pressure region (0–3 kPa) and $S_2 = 0.075$ kPa^{-1} in the high-pressure region (3–50 kPa).

This multistage behavior originates from the progressive compression mechanism. In the low-pressure regime, the porous hydrogel structure undergoes substantial deformation, leading to a dramatic increase in the contact area between MXene nanosheets and a sharp drop in resistance. As pressure increases (>3 kPa), the porous network becomes densified, and the resistance change is dominated by the intrinsic piezoresistive effect of the compact material, resulting in a stable but lower sensitivity.

The high S_1 enables the detection of subtle physiological signals (*e.g.*, pulse, touch), while the broad linear range of S_2 covers the entire spectrum of plantar pressures during walking.

Finally, long-term durability is a prerequisite for practical wearability. Fig. 5e presents the fatigue test of the sensor under repeated loading–unloading cycles at 200 kPa. The device maintained a highly stable output signal over 2500 cycles, without discernible baseline drift or signal degradation. The magnified insets (initial *vs.* final cycles) reveal that the waveform shape and amplitude remain consistent, confirming the exceptional mechanical elasticity and electrical reliability of the MXene-PAAc triple network. This robust fatigue resistance ensures the sensor's longevity for continuous gait monitoring tasks.

Biocompatibility evaluation

To comprehensively evaluate the biosafety of the MXene-PAAc hydrogel, the cytotoxicity towards L929 fibroblasts was assessed using the CCK-8 assay with hydrogel extracts, strictly adhering to the ISO 10993-5 standard.[48] As shown in the upper panels of Fig. 6, the quantitative cell viability was analyzed after culturing in hydrogel extracts with varying concentrations (0.1–100%). After 24 h of incubation, the hydrogel demonstrated exceptional biocompatibility, with cell viability maintaining above 99% across all groups. Notably, even the group treated with 100% undiluted extract exhibited a viability of 100.7%, showing no statistically significant difference compared to the

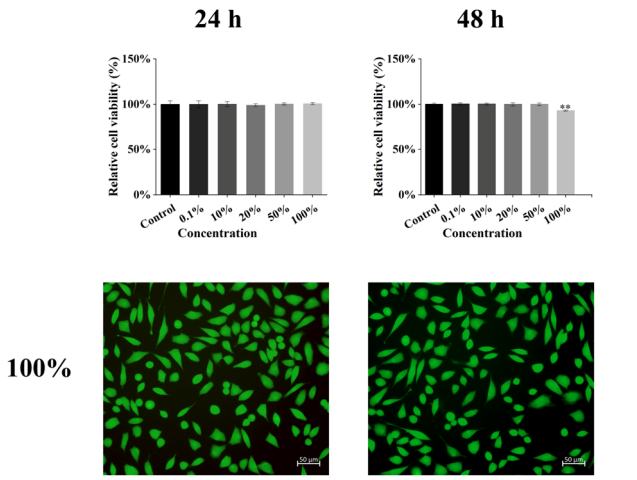

Fig. 6 *In vitro* cytocompatibility evaluation of MPG hydrogels using L929 fibroblasts. Quantitative cell viability determined by CCK-8 assay after incubation with different concentrations of hydrogel extracts for 24 h and 48 h (top row), and representative live/dead staining fluorescence images of cells treated with 100% hydrogel extract (bottom row; scale bar: 50 μm). Living cells are stained green (Calcein-AM), while dead cells are stained red (PI).

control group ($p > 0.05$). This suggests that any rapid release of potential leachables is negligible. When the incubation period was extended to 48 h, the viability of cells in the 0.1–50% concentration range remained stable at ≈ 100%. For the 100% extract group, a slight decrease in viability to 93.0% was observed. Although statistical analysis reveals a difference compared to the control ($p < 0.01$), this value far exceeds the internationally recognized safety threshold (>70% according to ISO 10993-5), confirming that the hydrogel maintains a high safety margin even under extreme concentrations and prolonged exposure.

The quantitative results are further corroborated by live/dead staining assays (Fig. 6, lower panels). The fluorescence images display the morphology of cells treated with the 100% extract. Even after 48 h of exposure to the undiluted extract, the cells displayed a high density of green fluorescence (live cells) with negligible red fluorescence (dead cells). The fibroblasts maintained a healthy, spindle-shaped morphology with extensive spreading, indicating that the material supports normal cell adhesion and proliferation without compromising membrane integrity.

In summary, the MPG hydrogel possesses superior biocompatibility, ensuring its suitability for reliable and safe long-term wearable applications.

Practical application

The application of flexible pressure sensors in plantar pressure monitoring is of great significance for early detection of diabetic foot ulcers, gait analysis, and rehabilitation assessment.[49] To evaluate the practical performance of the MPG hydrogel-based pressure sensor, the device was integrated into a customized smart insole system. As shown in Fig. 7a, the signal processing unit consists of an STM32 microcontroller, a Bluetooth module, and a portable battery pack. This compact system is designed to be wearable and strapped to the ankle (Fig. 7c), enabling unhindered movement during data acquisition. To achieve comprehensive gait analysis, eight independent MPG sensing units were strategically distributed across the key weight-bearing regions of the insole (Fig. 7b), specifically including four sensors on the forefoot (covering the metatarsals and toe area) to capture the push-off phase, two sensors on the midfoot (arch region) to monitor stability, and two sensors on the heel to detect the initial heel-strike impact. Each sensor was electrically connected to the processing unit *via* flexible wires soldered to the Cu foil electrodes, ensuring robust signal transmission. During walking experiments, the multi-channel system continuously recorded the resistance variations. As presented in Fig. 7d, the real-time response curves of all eight channels (L1–L8) exhibit stable and distinct cyclic patterns. The waveforms clearly delineate the sequential pressure distribution from the heel (initial contact) to the forefoot (propulsion), verifying the sensor's capability to capture high-resolution spatiotemporal gait features for the subsequent deep learning analysis.

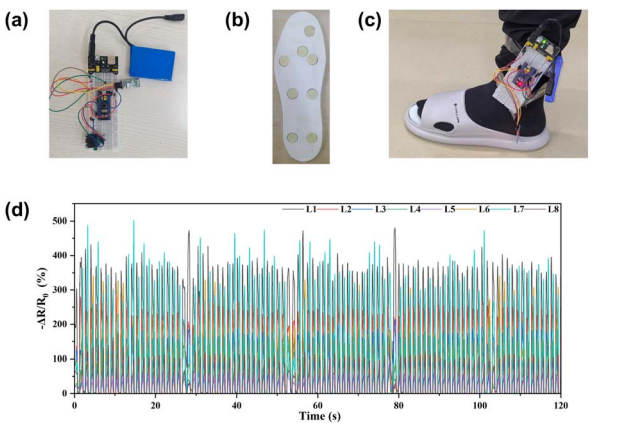

Fig. 7 (a) Photograph of the hardware components of the data acquisition module, (b) photograph of the insole integrated with the hydrogel-based pressure sensors, (c) demonstration of the foot-pressure measurement setup during testing, (d) dynamic resistance variation ($-\Delta R/R_0$) of the left foot sensors during the walking test.

Plantar pressure signal classification based on the CNN-LSTM hybrid model

Plantar pressure signals are inherently highly dynamic and complex time-series data, exhibiting only subtle morphological variations among different gait phases—heel strike (HS), foot flat (FF), mid-stance (MST), and toe-off (TO)—while being simultaneously influenced by individual gait characteristics, walking speed, and load variation.[50] Such signal complexity and inter-subject variability greatly reduce class separability. Conventional empirical or threshold-based detection methods often fail to accurately distinguish gait events. Although machine learning models such as random forests (RF) and support vector machines (SVM) can perform classification using handcrafted features, their reliance on feature engineering limits their ability to capture both local non-linear transitions and long-range tempor al dependencies, resulting in suboptimal classification performance.

The MPG hydrogel-based flexible pressure sensors provide high-fidelity plantar pressure signals, offering a reliable data foundation for intelligent gait recognition. To fully exploit the temporal dynamics of the signals, a convolutional neural network-long short-term memory (CNN-LSTM) hybrid model was developed. Plantar pressure signals possess dual feature characteristics: (i) instantaneous transitions, such as heel-strike and toe-off, which embody strong local nonlinearity, and (ii) cyclic temporal evolution throughout the gait process, reflecting global temporal dependencies. The CNN component extracts local spatial–temporal features and suppresses high-frequency noise, while the LSTM component effectively models long-term dependencies across gait cycles. Their integration enables joint representation of local fluctuations and global temporal patterns, thereby improving classification accuracy and robustness for complex dynamic signals.

Model performance and ablation validation. Under five-fold cross-validation, the proposed CNN-LSTM hybrid model demonstrated exceptional gait recognition capabilities. As summarized in Table 1 and Fig. 8, the model achieved a high average accuracy of 88.0% and a Macro-F1 score of 0.860. The

Table 1 Comparison of model performance metrics

Model	Accuracy	Macro F1	Weighted F1	Specificity (macro)	AUC (macro)	AUC (micro)
CNN-LSTM	0.880 ± 0.013	0.860 ± 0.023	0.884 ± 0.014	0.958 ± 0.007	0.980 ± 0.002	0.988 ± 0.002
CNN-Only	0.635 ± 0.043	0.280 ± 0.023	0.539 ± 0.049	0.781 ± 0.013	0.612 ± 0.046	0.814 ± 0.022
LSTM-Only	0.619 ± 0.052	0.231 ± 0.029	0.502 ± 0.069	0.766 ± 0.018	0.662 ± 0.045	0.819 ± 0.031
RF	0.646	0.337	0.578	—	0.709	0.842
SVM	0.666	0.370	0.601	—	0.748	0.855

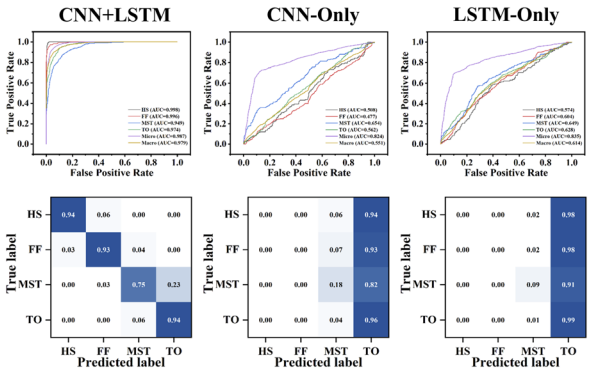

Fig. 8 Performance comparison of the proposed CNN-LSTM hybrid model against baseline models (CNN-Only and LSTM-Only) in gait phase recognition tasks. The top row displays the ROC curves for four gait phases (HS, FF, MST, TO), while the bottom row presents the corresponding confusion matrices. The columns from left to right represent the results for the CNN-LSTM, CNN-Only, and LSTM-Only models, respectively.

ROC curves (Fig. 8, upper panels) indicate robust generalization performance across all four gait phases (HS, FF, MST, TO), yielding a micro-average AUC of 0.987. Furthermore, the confusion matrices (Fig. 8, lower panels) confirm that the model maintains high recall rates even for the most challenging intermediate phases (*e.g.*, MST), effectively minimizing misclassification.

To further justify the necessity of the hybrid architecture (*i.e.*, to validate that the added computational complexity yields proportional performance gains), an ablation study was conducted to compare the hybrid model against single-stream CNN-Only and LSTM-Only baselines. The results reveal a substantial performance disparity: the CNN-Only model achieved an accuracy of only 63.5% (Macro-F1 = 0.280), while the LSTM-Only model reached just 61.9% (Macro-F1 = 0.231). This significant gap (≈25% improvement) highlights the inherent limitations of relying on a single feature extraction mechanism—CNNs lack long-range temporal modeling, while LSTMs are susceptible to high-frequency noise without spatial filtering.

Additionally, compared to traditional machine learning algorithms (RF: 64.6%; SVM: 66.6%, as shown in Fig. 9), the deep learning framework leverages automated feature extraction to capture complex non-linear dynamics, surpassing the limits of handcrafted features. Consequently, the CNN-LSTM architecture, by synergizing local spatial convolution with global temporal memory, provides a robust solution for precise gait analysis, fully justifying its architectural design.

In summary, the deep learning framework achieves high-precision recognition of complex gait dynamics through automated feature extraction and multi-scale temporal modeling. These results not only validate the feasibility of the MPG hydrogel-based sensors for real-time plantar pressure monitoring but also underscore their potential for intelligent gait analysis and wearable healthcare applications.

Experimental

Materials

Titanium aluminum carbide (Ti_3AlC_2, 99.8%, 200 mesh), lithium fluoride (LiF, ≥99.99%), gelatin (type A, 250 Bloom), acrylic acid (AAc, ≥99%, containing 180–220 ppm 4-methoxyphenol as an inhibitor), zirconium tetrachloride ($ZrCl_4$, ≥98%, Hf content ≤2%), and ammonium persulfate (APS, ≥98%) were all purchased from Aladdin Biochemical Technology Co., Ltd (Shanghai, China). All reagents were of analytical grade and used without further purification.

Preparation of MXene dispersion

To prepare the MXene dispersion, 2 g of LiF was dissolved in 40 mL of 9 M HCl solution and stirred at 50 °C for 15 min to

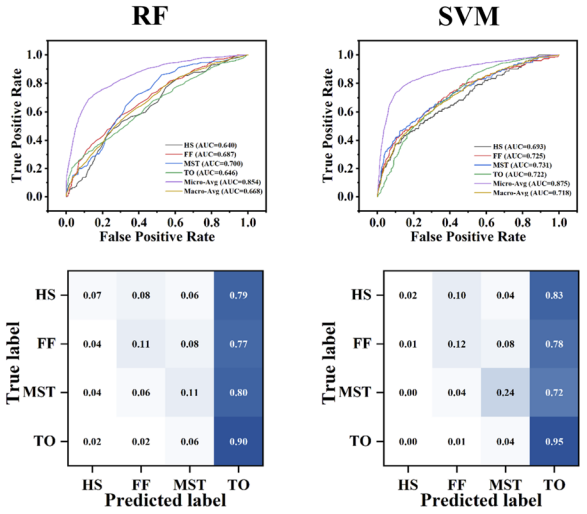

Fig. 9 Performance evaluation of traditional machine learning algorithms for gait phase recognition. The top row illustrates the ROC curves for the four gait phases (HS, FF, MST, TO), while the bottom row displays the corresponding confusion matrices. The columns represent the results for the Random Forest (RF) (left) and Support Vector Machine (SVM) (right) models, respectively.

form the etching medium. Subsequently, 2 g of Ti_3AlC_2 powder was slowly added within 5 min, and the mixture was continuously reacted for 48 h. After etching, the obtained suspension was centrifuged and washed 2–3 times with 2 M HCl, followed by repeated washing with deionized water until the supernatant reached pH > 6. The resulting supernatant containing delaminated $Ti_3C_2T_x$ nanosheets was collected to obtain the single-layer MXene dispersion.

Preparation of anti-swelling hydrogel

Gelatin (1 g) was dissolved in 9 mL of deionized water under continuous stirring at 50 °C for 30 min until completely dissolved. After cooling to room temperature, 1 mL of MXene dispersion (0, 2, 4, 6, 8, or 10 mg mL^{-1}), acrylic acid (AAc, 2 g), and zirconium tetrachloride ($ZrCl_4$, 4 wt% relative to AAc) were added to the gelatin solution. The mixed precursor was stirred for 30 min, followed by the rapid addition of ammonium persulfate (APS, 5 wt% of the total solution mass) as the initiator. After stirring for 15 s, the pregel solution was immediately poured into molds. Gelation was completed within 1 min at room temperature, and the resulting hydrogels were stored at 4 °C for 24 h to promote further formation of the gelatin network.

Fabrication of the hydrogel-based sensor

The pressure sensor was fabricated with a robust sandwich architecture, consisting of an MPG hydrogel sensing layer and flexible metallic electrodes. Ultrathin copper (Cu) foils (thickness ≈ 50 μm) were employed as current collectors to ensure stable electrical contact. The MPG hydrogel layer was sandwiched between two Cu foil electrodes. To ensure environmental stability, a frame of VHB acrylic elastomer tape (3M VHB) was employed as both a spacer and a sealant to bond the electrodes. This commercial elastomeric tape provides excellent adhesion and airtightness, effectively locking moisture within the hydrogel network to prevent dehydration, while simultaneously enhancing the structural integrity and mechanical resilience of the sensor under cyclic compression.

Characterization

The microstructure of MXene and the MPG composite hydrogel was examined using scanning electron microscopy (SEM, GeminiSEM 360, Zeiss, Germany). Prior to SEM observation, the hydrogel samples were freeze-dried and fractured in liquid nitrogen to expose their cross-sections, while MXene powders were directly mounted on conductive adhesive tape. The morphology of MXene nanosheets was characterized by transmission electron microscopy (TEM, JEOL JEM-F200, Japan). To analyze the crystalline structure, MXene films were obtained by vacuum filtration and tested using X-ray diffraction (XRD, Bruker D8 ADVANCE, Germany) with a scanning rate of 5° min^{-1} over the range of 5°–80°. The elemental composition and surface chemical states were determined by X-ray photoelectron spectroscopy (XPS, Thermo Fisher ESCALAB Xi+, USA). The electrical conductivity of the hydrogels was measured using a four-probe resistivity tester (ST2643, Jingge, China).

Mechanical property testing

The mechanical characterization was performed using specific testing systems depending on the deformation mode. Tensile properties were evaluated using a universal testing machine (UTM5105, Sansi Zongheng, China), where rectangular specimens with dimensions of 75 mm × 12.5 mm × 2 mm were stretched at a crosshead speed of 30 mm min^{-1}. For compression performance, a tester (ZQ-990A, Zhiqu, China) was employed. Cylindrical samples were prepared by casting the precursor solution into a 24-well culture plate serving as the mold. Static compression stress–strain curves were recorded under a maximum stress of 0.5 MPa, while cyclic loading–unloading fatigue tests were conducted at a fixed pressure of 200 kPa for 2500 cycles.

Sensing performance evaluation

The electromechanical sensing performance of the MPG hydrogel sensors was evaluated using a universal testing machine (ZQ-990A, Zhiqu, China) coupled with a digital source meter (S100B, Precise, China). For sensitivity measurements, cylindrical hydrogel specimens were prepared with a diameter of 10 mm and a height of 20 mm. The real-time resistance variation was recorded under applied pressures ranging from 0 to 50 kPa, and the sensitivity (S) was calculated using the equation:

$$S = \frac{\Delta R/R_0}{\Delta P}$$

where R_0, ΔR, and ΔP denote the initial resistance, resistance change, and applied pressure variation, respectively. Separately, to assess the long-term electrical stability and fatigue resistance, cyclic loading–unloading tests were performed on samples prepared using 24-well culture plates (consistent with mechanical characterization). These durability tests were conducted at a fixed pressure of 200 kPa for 2500 cycles, during which the electrical resistance response was synchronously monitored.

Anti-swelling test

To evaluate the anti-swelling performance of the MXene-PAAc-gelatin composite hydrogel, samples were cut into cubic specimens with approximately identical dimensions (10 mm × 10 mm × 3 mm). The initial weight of each sample (W_0) was recorded. The specimens were then immersed in deionized water at room temperature (25 ± 1 °C) and allowed to swell under static conditions. At predetermined intervals, the samples were taken out, gently blotted with filter paper to remove surface moisture, and weighed to obtain the transient mass (W_t).

The swelling degree (SD_{30d}) was calculated according to the following equation:

$$SD_{30d}(\%) = \frac{W_{30d} - W_0}{W_0} \times 100\%$$

(Note: W_{30d} represents the weight recorded on Day 30.)

To assess the stability under physiological pH variations, the optimized hydrogel (6 mg MXene) was immersed in buffer solutions with pH values of 3, 5, 7, and 9. The weight variation was monitored daily for 30 days. The Swelling Ratio (SR) was defined as the ratio of the transient weight to the initial weight to quantify the gravimetric stability under different osmotic conditions:

$$\mathrm{SR}\left(\mathrm{g\ g^{-1}}\right) = \frac{W_t}{W_0}$$

Each measurement was repeated three times for each sample group, and the average value was reported as the final result.

Biocompatibility evaluation

***In vitro* cytotoxicity evaluation.** To assess the potential risk of skin irritation, the cytocompatibility of the MPG hydrogels was evaluated using L929 mouse fibroblasts (Procell, Wuhan, China) in accordance with the ISO 10993-5 standard.

Sample preparation. Sterilized hydrogel samples were immersed in MEM complete medium (Procell) supplemented with 10% fetal bovine serum (FBS, Sangon Biotech) at a mass-to-volume ratio of 0.1 g mL^{-1}. The extraction was conducted at 37 °C for 24 h, and the supernatant was filtered for sterilization to obtain the hydrogel extracts.

Quantitative analysis (CCK-8 assay). L929 cells were seeded into 96-well plates at a density of 4×10^3 cells per well and incubated for 24 h. Subsequently, the culture medium was replaced with 100 μL of the hydrogel extracts (or diluted working solutions), while fresh complete medium served as the control group. After incubation for 24 and 48 h, cell viability was quantified using the Cell Counting Kit-8 (CCK-8, Sangon Biotech). The optical density (OD) was measured at 450 nm using a microplate reader (SpectraMax Paradigm, Molecular Devices, USA). Cell viability was calculated as:

$$\text{Cell viability}(\%) = \frac{\mathrm{OD_{sample}}}{\mathrm{OD_{control}}} \times 100\%$$

Qualitative analysis (live/dead staining). Cell morphology and viability were visually assessed using a Calcein-AM/PI Cell Viability and Cytotoxicity Assay Kit (Beyotime, Shanghai, China). Cells were seeded in confocal dishes and treated with 100% hydrogel extracts for 24 and 48 h. After washing with PBS, the cells were stained with a working solution containing 2 μM Calcein-AM (staining living cells green) and 8 μM Propidium Iodide (PI, staining dead cells red). The samples were incubated for 30 min at 37 °C in the dark and subsequently visualized using an inverted fluorescence microscope.

Data preprocessing

The plantar pressure signals were collected using an insole-type sensor array. The raw data were first denoised and normalized to eliminate baseline drift and inter-channel variations. Subsequently, a sliding window segmentation approach was applied with a window size of 200 and a step size of 50. Within each gait cycle, four gait events—Heel Strike (HS), Foot Flat (FF), Mid-Stance (MST), and Toe Off (TO)—were used as class labels. To address class imbalance, data augmentation techniques were employed to expand the minority classes, ensuring a relatively uniform class distribution across the dataset.

CNN-LSTM model and comparative experiments

A hybrid CNN-LSTM model was developed to effectively extract both local and temporal dependencies from plantar pressure signals. The model architecture consisted of two one-dimensional convolutional layers for hierarchical temporal feature extraction, followed by a two-layer long short-term memory (LSTM) network to capture long-range temporal correlations. The final classification was performed through a fully connected layer.

Model training was conducted using the Adam optimizer with a learning rate of 1×10^{-4}, a batch size of 64, and 50 training epochs. To ensure generalization, a fivefold cross-validation strategy was adopted, guaranteeing that data from the same subject did not simultaneously appear in both the training and validation sets.

For comparison, traditional machine learning models including Random Forest (RF) and Support Vector Machine (SVM) were implemented. The input features comprised statistical descriptors such as mean, standard deviation, extrema, and signal energy within each time window.

Furthermore, to rigorously validate the necessity of the hybrid architecture and evaluate the specific contributions of its components, a comprehensive ablation study was conducted. Two single-stream baseline models were constructed: (i) a CNN-Only model, which retained the convolutional layers for feature extraction but excluded the recurrent units, and (ii) an LSTM-Only model, which processed the raw time-series sequences using the identical LSTM structure without prior spatial filtering. These ablation baselines were trained and evaluated under identical hyperparameters and cross-validation protocols to ensure a fair comparison.

Model performance was comprehensively evaluated using multiple metrics, including overall accuracy, precision, recall, specificity, macro-averaged F1 score (Macro-F1), and weighted-averaged F1 score (Weighted-F1). Additionally, confusion matrices and multiclass receiver operating characteristic (ROC) curves were plotted, and both macro-AUC and micro-AUC values were calculated to assess the classification robustness.

Conclusions

In summary, a high-performance MPG composite hydrogel was successfully fabricated *via* a facile one-pot strategy. The synergistic cross-linking between MXene nanosheets and Zr^{4+} ions significantly enhanced the mechanical robustness, electrical conductivity, and, notably, the anti-swelling stability of the hydrogel. Among the prepared samples, the hydrogel with an MXene concentration of 6 mg mL^{-1} exhibited the optimal overall performance. Based on this optimized material, a flexible pressure sensor was constructed, demonstrating high

sensitivity, a rapid response time (92/129 ms), and a broad detection range. When integrated into a smart insole system, the device achieved real-time plantar pressure monitoring and accurately characterized sequential gait phases during walking. Furthermore, the proposed CNN-LSTM hybrid model effectively integrated local feature extraction and temporal dependency modeling, yielding an exceptional classification accuracy of 88% compared with conventional machine learning algorithms. These findings not only validate the practical applicability of the MPG hydrogel-based sensor but also provide a new paradigm for intelligent wearable devices in the early detection of diabetic foot ulcers, gait analysis, and rehabilitation medicine.

Author contributions

Q. W. conceived the concept, conducted the experiments, and drafted the manuscript. F. C., C. T., H. K., X. W., and X. C. contributed to the data analysis and sample characterization. L. Q. and S. X. provided supervision and critically revised the manuscript. All authors reviewed and approved the final version.

Conflicts of interest

There are no conflicts to declare.

Data availability

The data supporting the material characterization and model parameters are included in the article. The raw sensor data collected from human participants are not publicly available due to privacy and ethical restrictions.

Acknowledgements

This work was supported by Hebei Provincial Key R&D Program (22371301D); Chengde Municipal Science and Technology Program (202304B046, 202305B008); Hebei Provincial Foreign Intelligence Introduction Project; Research and Development of 3D Printed Hydrogel-Based Skin Sensors (KY202403).

Notes and references

1 J. Ma, H. Liang, W. Li, E. Liang and W. Zhang, *ACS Appl. Polym. Mater.*, 2025, **7**, 4549–4560.
2 Y. Gao, L. Yu, J. C. Yeo and C. T. Lim, *Adv. Mater.*, 2020, **32**, 1902133.
3 Z. Chen, C. Qu, J. Yao, Y. Zhang and Y. Xu, *ACS Appl. Mater. Interfaces*, 2024, **16**, 7640–7649.
4 J. Wu, Z. Mo, X. Gao, W. Xin, W. Shi and J. Park, *Int. J. Smart Nano Mater.*, 2025, **16**, 510–548.
5 R. Yin, D. Wang, S. Zhao, Z. Lou and G. Shen, *Adv. Funct. Mater.*, 2021, **31**, 2008936.
6 H. Yuk, B. Lu and X. Zhao, *Chem. Soc. Rev.*, 2019, **48**, 1642–1667.
7 E. M. Ahmed, *J. Adv. Res.*, 2015, **6**, 105–121.
8 X. Liu, J. Liu, S. Lin and X. Zhao, *Mater. Today*, 2020, **36**, 102–124.
9 G. Ge, Y. Zhang, J. Shao, W. Wang, W. Si, W. Huang and X. Dong, *Adv. Funct. Mater.*, 2018, **28**, 1802576.
10 A. Roy, S. Zenker, S. Jain, R. Afshari, Y. Oz, Y. Zheng and N. Annabi, *Adv. Mater.*, 2024, **36**, 2404225.
11 L. Wang, T. Xu and X. Zhang, *TrAC, Trends Anal. Chem.*, 2021, **134**, 116130.
12 Z. Nie, K. Peng, L. Lin, J. Yang, Z. Cheng, Q. Gan, Y. Chen and C. Feng, *Chem. Eng. J.*, 2023, **454**, 139843.
13 L. Hu, P. L. Chee, S. Sugiarto, Y. Yu, C. Shi, R. Yan, Z. Yao, X. Shi, J. Zhi, D. Kai, H. Yu and W. Huang, *Adv. Mater.*, 2023, **35**, 2205326.
14 J. Li, T. Xu, Z. Ma, W. Li, Y. Qian, Y. Tao, Y. Wei, Q. Jiang, Y. Luo and J. Yang, *Energy Environ. Mater.*, 2024, **7**, e12547.
15 X. Yu, Y. Zheng, H. Zhang, Y. Wang, X. Fan and T. Liu, *Chem. Mater.*, 2021, **33**, 6146–6157.
16 M. Chen, W. Qin, Y. Wang, Y. Song, F. Tian, H. Zhai, C. Gu, L. Ge, S. Xue, X. Li, X. Zhao, Y. Xu, Z. Ming, S. Li and S. Yin, *Sens. Actuators, B*, 2025, **444**, 138385.
17 G. Wang, Q. Zhang, Q. Wang, L. Zhou and G. Gao, *ACS Appl. Mater. Interfaces*, 2021, **13**, 24173–24182.
18 Z. Zhang, B. Feng, J. Yan, W. Zhao and J. Sun, *Green Chem.*, 2025, **27**, 1604–1619.
19 M. Yang, Y. Cheng, Y. Yue, Y. Chen, H. Gao, L. Li, B. Cai, W. Liu, Z. Wang, H. Guo, N. Liu and Y. Gao, *Adv. Sci.*, 2022, **9**, 2200507.
20 X. Yuan, Z. Zhu, P. Xia, Z. Wang, X. Zhao, X. Jiang, T. Wang, Q. Gao, J. Xu, D. Shan, B. Guo, Q. Yao and Y. He, *Adv. Sci.*, 2023, **10**, 2301665.
21 F. Zheng, X. Yang, J. Li, Z. Tian, B. Xiao, S. Yi and L. Duan, *Int. J. Biol. Macromol.*, 2022, **205**, 595–603.
22 U. Amara, L. Xu, I. Hussain, K. Yang, H. Hu and D. Ho, *Small*, 2025, **21**, 2405047.
23 R. Qin, J. Nong, K. Wang, Y. Liu, S. Zhou, M. Hu, H. Zhao and G. Shan, *Adv. Mater.*, 2024, **36**, 2312761.
24 Q. Lai, X. Zhao, Q. Sun, Z. Tang, X. Tang and V. A. L. Roy, *Small*, 2023, **19**, 2300283.
25 M. Pi, S. Qin, S. Wen, Z. Wang, X. Wang, M. Li, H. Lu, Q. Meng, W. Cui and R. Ran, *Adv. Funct. Mater.*, 2023, **33**, 2210188.
26 D. Boateng, X. Li, Y. Zhu, H. Zhang, M. Wu, J. Liu, Y. Kang, H. Zeng and L. Han, *Biosens. Bioelectron.*, 2024, **261**, 116499.
27 T. Sun, B. Feng, J. Huo, Y. Xiao, W. Wang, J. Peng, Z. Li, C. Du, W. Wang, G. Zou and L. Liu, *Nano-Micro Lett.*, 2024, **16**, 14.
28 X. Kong, W. Wen, Y. Guan, Z. Lin, J. Zheng, B. Xie, S. Li, J. Xue and Q. Hu, *ACS Appl. Mater. Interfaces*, 2025, **17**, 31778–31798.
29 L. Yang, O. Amin and B. Shihada, *ACM Comput. Surv.*, 2024, **56**, 1–42.
30 W. Wang, H. Zhou, Z. Xu, Z. Li, L. Zhang and P. Wan, *Adv. Mater.*, 2024, **36**, 2401035.
31 C. Yang, D. Zhang, D. Wang, H. Luan, X. Chen and W. Yan, *ACS Appl. Mater. Interfaces*, 2023, **15**, 5811–5821.
32 B. Gurzęda, N. Boulanger, A. Nordenström, C. Dejoie and A. V. Talyzin, *Adv. Sci.*, 2024, **11**, 2408448.

33 V. Natu, M. Benchakar, C. Canaff, A. Habrioux, S. Célérier and M. W. Barsoum, *Matter*, 2021, **4**, 1224–1251.
34 P. Ma, W. Liang, R. Huang, B. Zheng, K. Feng, W. He, Z. Huang, H. Shen, H. Wang and D. Wu, *Adv. Mater.*, 2024, **36**, 2305400.
35 X. Guan, M. Bi, S. Sun, Y. Yang, J. Sun, Z. Jin, H. Ren and Z. Gao, *J. Mater. Chem. B*, 2024, **12**, 7420–7428.
36 H. Fang, T. Dong, Z. Yuan, X. Zhang and W. Shao, *Chem. Eng. J.*, 2025, **518**, 164546.
37 Y.-Z. Zhang, K. H. Lee, D. H. Anjum, R. Sougrat, Q. Jiang, H. Kim and H. N. Alshareef, *Sci. Adv.*, 2018, **4**, eaat0098.
38 J. H. Cavka, S. Jakobsen, U. Olsbye, N. Guillou, C. Lamberti, S. Bordiga and K. P. Lillerud, *J. Am. Chem. Soc.*, 2008, **130**, 13850–13851.
39 *Handbook of X-ray Photoelectron Spectroscopy*, ed. J. Chastain and R. C. King Jr, Perkin-Elmer Corporation, 1992, vol. 40, p. 25.
40 Y. Zhang, M. Gong and P. Wan, *Matter*, 2021, **4**, 2655–2658.
41 K. Y. Li, D. H. Yang, C. Liu, W. Jiang, Y. Liu, H. Y. Yang, B. Wang and Y. Fu, *Int. J. Biol. Macromol.*, 2025, **329**, 147784.
42 Y. Yu, H. Yuk, G. A. Parada, Y. Wu, X. Liu, C. S. Nabzdyk, K. Youcef-Toumi, J. Zang and X. Zhao, *Adv. Mater.*, 2019, **31**, 1807101.
43 J. Zhang, Y. Hu, L. Zhang, J. Zhou and A. Lu, *Nano-Micro Lett.*, 2023, **15**, 8.
44 Y. Yang, N. Wu, B. Li, W. Liu, F. Pan, Z. Zeng and J. Liu, *ACS Nano*, 2022, **16**, 15042–15052.
45 Y. Yang, Y. Yang, Y. Cao, X. Wang, Y. Chen, H. Liu, Y. Gao, J. Wang, C. Liu, W. Wang, J.-K. Yu and D. Wu, *Chem. Eng. J.*, 2021, **403**, 126431.
46 Z. Hadi, J. Khademzadeh Yeganeh, M. Tajammal Munir, Y. Zare and K. Yop Rhee, *Composites, Part A*, 2024, **186**, 108422.
47 S. Zhang, F. Guo, M. Li, M. Yang, D. Zhang, L. Han, X. Li, Y. Zhang, A. Cao and Y. Shang, *J. Colloid Interface Sci.*, 2024, **658**, 137–147.
48 International Organization for Standardization, *ISO 10993-5: Biological Evaluation of Medical Devices – Part 5: Tests for in Vitro Cytotoxicity*, International Organization for Standardization, Geneva, 2009.
49 C. Wang, D. Gong, P. Feng, Y. Cheng, X. Cheng, Y. Jiang, D. Zhang and J. Cai, *ACS Appl. Mater. Interfaces*, 2023, **15**, 8546–8554.
50 F. Mun and A. Choi, *J. NeuroEng. Rehabil.*, 2022, **19**, 4.